Journal of Materials Chemistry A

Accepted Manuscript

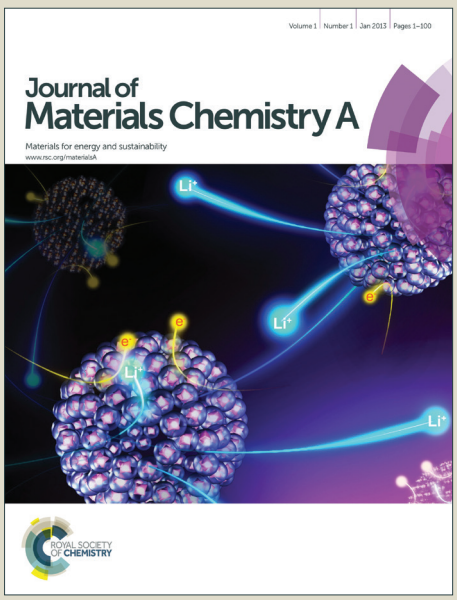

ROYAL SOCIETY OF CHEMISTRY

www.rsc.org/materialsA

Mesoporous size controllable carbon microspheres and their electrochemical performances for supercapacitor electrodes

Xiaomei Ma, Lihua Gan*, Mingxian Liu*, Pranav K. Tripathi, Yunhui Zhao, Zijie Xu, Dazhang Zhu and Longwu Chen

In this paper, size controllable SiO_2 nanoparticles synthesized by adjusting hydrolysis-condensation time and concentration of tetraethyl orthosilicate (TEOS) in ethanol/water solution with the present of ammonia as catalyst were encapsulated within resorcinol/formaldehyde polymer microspheres which fabricated in the same ethanol/water/ammonia system. After carbonization and following etching with NaOH solution, a series of mesoporous carbon microspheres (MCMs) with average diameter of 500 nm, mesopore size of 3.2-14 nm and surface areas of 659-872 m^2 g^{-1} are obtained. As electrode materials for supercapacitor, typical samples of MCMs with mesopore size of 3.2 nm and 13.5 nm show initial specific capacitance of 289 and 268 F g^{-1} under a current density of 1.0 A g^{-1}. After 10000 charge-discharge cycles, the specific capacity remains 261 and 254 F g^{-1} with the retention of 90.3% and 94.7%. Besides, electrochemical performances influenced by mesoporous size were investigated.

1. Introduction

Supercapacitors or electric double-layer capacitors (EDLC) are a new energy storage system, which combine the superiority of high power dielectric capacitor and high specific energy of rechargeable batteries.[1-4] Supercapacitors also play an important role in power sources and applied in hybrid electric vehicles and short-term power sources for mobile electric devices.[5-8]

The energy storage of supercapacitors based on double-layer capacitance which is the accumulation of ionic charges located at the electrode/electrolyte interface,[9-11] thus, a high specific surface area and moderate pore size distribution of porous carbon materials electrode are the optimal selection for achieving high-performance supercapacitor.[12-14] Microporous carbon materials such as activated carbon with higher specific surface area can provide abundant adsorbing sites for active ions and enhance the electrochemical capacitance.[15,16] Unfortunately, the irregular and island-like microporous structure in activated carbons resulted in poor accessibility of electrolyte ions into the porous surface, and such a disadvantage causes much difficulty to achieve proportionality between their electrochemical capacitances and surface areas, especially in the case of a relatively high loading current density.[17] Mesoporous carbon is one of the most commonly used electrode materials for supercapacitor due to their high specific surface area, abundant mesoporous structure, and appropriate mesopore size (2-50 nm) which afford facile diffusion of electrolyte ion and mass transfer (i.e., fast diffusion of electrolytes through large pores) where a fast charge/discharge needed.[18,19] In general, synthesis of mesoporous carbon relies on the ways of nanocasting pathway and self-assembly approaches. For example, Li et al synthesized ordered mesoporous carbons by using furfuryl alcohol as the carbon source and SBA-15 as a template.[20] Kong et al prepared carbon/silica matrix using resorcinol/formaldehyde as precursor templated by 3-aminopropyl-triethoxysilane,[21] if the silica were removed by HF or NaOH, carbon material with porous structure will be obtained. Xu et al reported a self-assembly method for synthesis of ordered mesoporous carbon using F127 and resorcinol-formaldehyde resol.[22] Fulvio et al fabricated mesoporous carbon nanocomposites by a “Brick-and-Mortar” self-assembly

approach.[23] These methods provided many famous mesoporous or ordered mesoporous carbon with high specific surface areas and excellent mesoporous structures. However, these techniques have an important drawback that they are very effective to obtain mesoporous with a single pore size, but they are not so versatile as to produce a series of pore size controllable carbon materials by controlling the size of a single template in one synthesis route. Therefore, it is meaningful that carbon materials with different mesoporous size structure are expected to investigate their influences on electrochemical performances of a superior electrode material for supercapacitor application.

Stöber method is very famous for the preparation of SiO_2 spheres.[24] Liu et al. synthesized monodisperse resorcinol/formaldehyde polymer and carbon spheres by extension of the Stöber method.[25] Fuertes et al. prepared core@shell spheres through a thin layer of resorcinol/formaldehyde polymer enveloping a silica core by one-step method under Stöber conditions.[26] Liu et al. fabricated mesoporous polymeric and carbonaceous nanospheres by an extended Stöber method with a facile soft-template (cationic fluorocarbon surfactant FC4, triblock copolymer Pluronic F127).[27] In our previous work, uniform polymer and carbon nanospheres with tunable sizes were fabricated by a novel seeded synthetic strategy. Phloroglucinol and terephthalaldehyde were polymerized to form colloidal seeds, and then resorcinol/formaldehyde reacted on the seed surface to assemble polymer nanospheres with tunable sizes via time-controlled formation of colloidal seeds.[28] In addition, mesoporous carbon microspheres using colloidal SiO_2 template following KOH activation was also reported in our study.[29] Therefore, fabrication of porous size controllable carbon nanospheres by using SiO_2 template that obtained in the same synthesis condition is the motivation and

objective of this work. Herein, we demonstrate the design and fabrication of SiO_2 nanoparticles with different size by controlling hydrolysis-condensation time and concentration of tetraethyl orthosilicate (TEOS) in ethanol/water solution with ammonia as catalyst. SiO_2 nanoparticles were encapsulated within resorcinol/formaldehyde polymer microspheres which synthesized in the same ethanol/water/ammonia system, and SiO_2/RF polymer microspheres were obtained. After carbonization and SiO_2 template remove process, a series of MCMs with different pore size were produced. This method develops a simple route for the synthesis of pore size controllable carbon spheres, and study the electrochemical performances based on pore size influence will be discussed in detail.

2. Experimental

2.1 Materials

All the chemicals and reagents were of analytical grade and were used without further purification. Resorcinol (R), formaldehyde (F) (37 wt.%), ethanol (99 wt.%), ammonia solution (25 wt.%) and NaOH (solid state) were purchased from Sinopharm Chemical Reagent Co., Ltd. Shanghai, China. Tetraethyl orthosilicate (TEOS) was supplied by Aladdin Reagent Co., Ltd. Shanghai, China. Polytetrafluoroethylene (catalog number FR301B) was purchased from Shanghai 3F New Materials Co., Ltd. Nickel foil was obtained from Shanghai Hongxiang Plant. Pure nitrogen was provided by Shanghai BOC Special Gases Sales Service Co., Ltd.

2.2 Synthesis of MCMs

Particles sizes of nano-SiO_2 were controlled in synthesis procedure by adjusting

hydrolysis-condensation time and concentration of TEOS in the ethanol/water/ammonia system. For a solvent condition, 110 mL of deionized water, 45 mL of ethanol and 1.5 mL of ammonia were mixed under stirring for 1 h. Then, stoichiometric amount of TEOS was added and stirring for a certain time, resorcinol was added and stirring for 10 min. Finally, formaldehyde was dropwise added into the above mixture and lasting stirring for 24 h at 30 °C to prepare SiO_2/RF polymer. The obtained product was transferred into 100 mL Teflon container at 100 °C for 24 h, and SiO_2/RF polymer microspheres were obtained. After dying, the SiO_2/RF polymer microspheres was placed in a tube furnace and carbonized at 850 °C with a heating rate of 3 °C min^{-1} under nitrogen atmosphere to obtain SiO_2/Carbon. SiO_2 encapsulated in carbon microspheres were etched by 3 M NaOH solution and the resultant products were called MCM-x-y, where x denotes the hydrolysis-condensation time, y is the stoichiometric amount of TEOS. Details of synthesis conditions and textural parameters of MCM-x-y were listed in Table 1.

Table1. Synthesis conditions and textural parameters of MCMs

Sample	Time (min)	TEOS (g)	R (g)	F (mL)
MCM-30-2.0	30	2.0	1.0	1.4
MCM-30-2.5	30	2.5	1.02	1.45
MCM-50-4.0	50	4.0	1.05	1.5
MCM-50-5.0	50	5.0	1.08	1.5
MCM-70-5.5	70	5.5	1.1	1.6
MCM-70-6.3	70	6.3	1.2	1.6

2.3 Characterization

Scanning electron microscopy (SEM) images were taken in JSM-6700F equipment. N_2 adsorption and desorption isotherms were obtained at -196 °C using Micromeritics Tristar

3000 gas adsorption analyzer. Before measurements, the samples were degassed at 200 °C under vacuum for more than 2 h. The specific surface area was calculated by Brunauer-Emmett-Teller (BET) method. The pore size distributions were estimated by Barrett-Joyner-Halenda (BJH) model by using the adsorption branch of the isotherms. The total pore volume was determined from the adsorbed amount at a relative pressure of P/P_0=0.98. Power X-ray diffraction (XRD) patterns were obtained on a Bruker Focus D8 diffract-meter with Cu Kα radiation (40 kV, λ=0.15418 nm) between 10 and 90°. Raman spectra were recorded using Invia instrument with a 520 nm Ar-ion laser.

2.4 Electrochemical measurements

The electrochemical performances including cyclic voltammetry (CV), galvanostatic charge/discharge (GCD) and electrochemical impedance spectroscopy (EIS) were conducted in a CHI 660D instrument with a typical three-electrode system. Hg/HgO electrode was used as a reference electrode, and nickel foam as a counter electrode.[30] The working electrode was prepared by mixing as-prepared carbon material, graphite, and polytetrafluoroethylene with a mass ratio of 8:1:1 in a required amount of ethanol to form a paste.[30] Then, the paste with a thickness of 1 mm was pressed into the nickel foam and served as a working electrode which was soaked in 6 M KOH solution for 24 h to facilitate the electrolyte completely diffuse into the pores of materials.

3. Results and discussion

Fabrications of size controllable SiO_2 nanoparticles and mesoporous carbon microspheres are shown in Scheme 1. Hydrolysis-condensation of TEOS in ethanol/water solution with the presence of ammonia by sol-gel process leads to the formation of monodisperse spherical

SiO_2 nanoparticles.[24,31] The size of SiO_2 nanoparticle depends upon hydrolysis-condensation time and concentration of TEOS added in the ethanol/water/ ammonia solution. There are three steps to explain the formation and growth of SiO_2 nanoparticles (Scheme 1A). The first step is the monomer addition growth model, which involves nucleation upon exceeding the supersaturating limit and nucleus growth by condensation of monomeric silicic acid on the surface of the existing particles (First stage of growth). The second step implies the controlled aggregation of sub-nanoparticles. The particles growth mechanism changes at a later stage during the hydrolysis-condensation reaction influenced by time and concentration of TEOS, and, hence, particles grow solely by condensation of monomeric and dimeric silicate units on the particle surface (Second stage of growth).[32] Further, when increase the hydrolysis-condensation reaction time and concentration of TEOS, a layer of tight aggregated particles cover in the surface of SiO_2 nanoparticles formed in the second stage of growth. Therefore, the relative larger size of SiO_2 nanoparticles obtained (Third stage of growth).

Scheme 1B illustrates the mechanism proposed for preparation of SiO_2/RF microspheres. RF polymer microspheres can be obtained according to the hydrolysis polymerization reaction mechanism of resorcinol/formaldehyde resins by sol-gel process in the similar ethanol/water/ammonia system.[25,33] After the SiO_2 nanoparticles are rapidly generated in Scheme 1A, NH_4^+ ions cover in the surface of SiO_2 nanoparticles (negatively charged) thereby preventing their aggregation and allowing the formation of a stable colloidal SiO_2. When resorcinol and formaldehyde were added, there occurs a polymer reaction between the resorcinol and formaldehyde which was catalyzed by OH^- ions.[28] As a result, hydroxymethyl-substituted species are formed, and a large number of

resorcinol/formaldehyde polymer forming onto the surface of SiO_2 nanoparticles due to the electrostatic interaction with the NH_4^+ ions existence. Therefore, the SiO_2 nanoparticles with several nanometers were entrapped in resorcinol/formaldehyde polymer microspheres under the same solution and synthesis condition. After carbonization and etched with NaOH, carbon microspheres with different pore sizes are obtained.

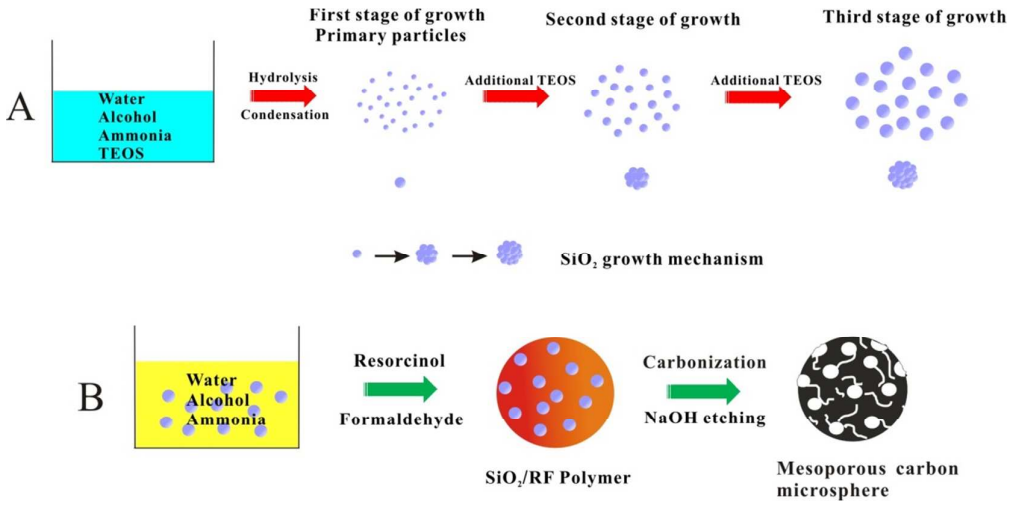

Scheme 1. Schematic illustration for preparation of SiO_2 nanoparticles and fabrication of mesoporous carbon microspheres.

Figure 1a-d show the SEM images of as-prepared MCMs, noting that the morphology of the MCMs are regularly and uniform monodisperse microspheres with average diameters of about 500 nm. It is found that the sizes of carbon microspheres are constant while controlling the nanoparticle size of SiO_2 by increasing the hydrolysis-condensation time and concentration of TEOS in the ethanol/water/ammonia solution. FESEM images set in Figure 1 a-d reveal the enlarged single MCMs, the rough surface indicate the porous structure which produced by remove of SiO_2 particles and framework shrink after RF decomposition. TEM images of MCMs are presented in Figure 2. These MCMs show obvious mesopores inside the

carbon matrix which could be ascribed to the removal of silica nanoparticles. It could be concluded from Figure 2a to Figure 2f that the pore size of the carbon microspheres could be controllable by the size of SiO_2 nanoparticles which is adjustable by changing the hydrolysis-condensation condition of TEOS in ethanol/water/ammonia solution.

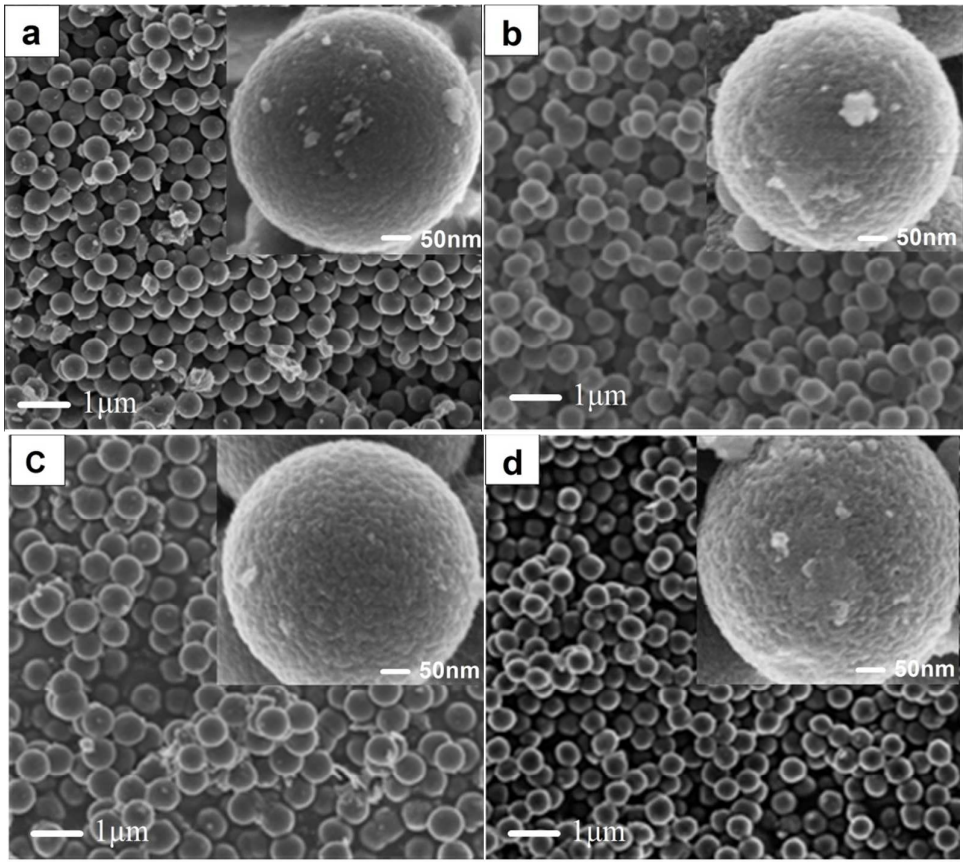

Figure 1. FESEM images of MCMs: (a) MCM-30-2.5; (b) MCM-50-5.0; (c) MCM-70-5.5; and (d) MCM-70-6.3.

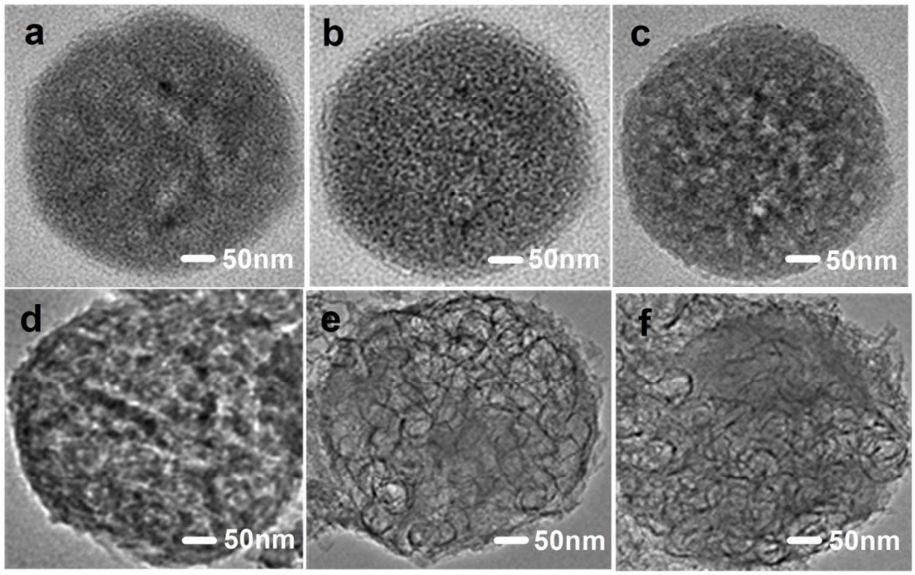

Figure 2. TEM images of MCMs: (a) MCM-30-2.0; (b) MCM-30-2.5; (c) MCM-50-4.0; (d) MCM-50-5.0; (e) MCM-70-5.5; and (f) MCM-70-6.3.

Nitrogen adsorption-desorption isotherms and pore size distribution profiles of MCMs are shown in Figure 3. From Figure 3a, it can be seen all of samples exhibit type-IV curves with a sharp capillary condensation at high relative pressures, obvious hysteresis loops observed in the adsorption-desorption isotherms indicating the existence of mesoporous structure in MCMs.[34] The pore size distribution profiles of MCMs calculated from the adsorption branches of isotherms by using the BJH model are shown in Figure 3b.[35] MCM-30-2.0 and MCM-30-2.5 show a pore size of 3.2 and 5 nm, respectively, which derives from the removal of the SiO_2 nanoparticles formed at the first stage. Through the hydrolysis-condensation of additional TEOS onto the surface of SiO_2 nanoparticles (the second stage), MCM-50-4.0 and MCM-50-5.0 present the mesopore size of 8.5 and 10 nm. Representative TEM images of SiO_2 nanoparticles formed at the second stage were shown in Figure 3c-d. The SiO_2 nanoparticles templated for MCM-50-4.0 and MCM-50-5.0 have a diameter of about 9 and 12

nm, which basically correspond to the pore size of MCM-50-4.0 and MCM-50-5.0 shown in Figure 3b. With further increase the hydrolysis-condensation time of TEOS on the basis of the second stage, additional silica grow onto the surface of the matrix nanoparticles (8.5, 10 nm). Consequently, the resultant MCM-70-5.5 and MCM-70-6.3 show bigger mesopore size of 13.5 and 14 nm. This result indicates that the mesoporous size of MCMs could be controllable by adjusting the sizes of silica nanoparticles which are dependent on the specific hydrolysis-condensation condition such as time, step and concentration. The specific surface area, pore size and pore volume of MCMs are presented in Table 2. The samples show total surfaces areas of 564-872 m^2 g^{-1} with mesporous surface areas of 370-416 m^2 g^{-1} and total pore volume of 0.59-0.74 cm^3 g^{-1}. Microporous surface areas of 289-452 m^2 g^{-1}, which affords nearly a half proportion of specific areas was attributed to the decomposition of RF polymer which sent off some low molecular weight components during the carbonization.[36]

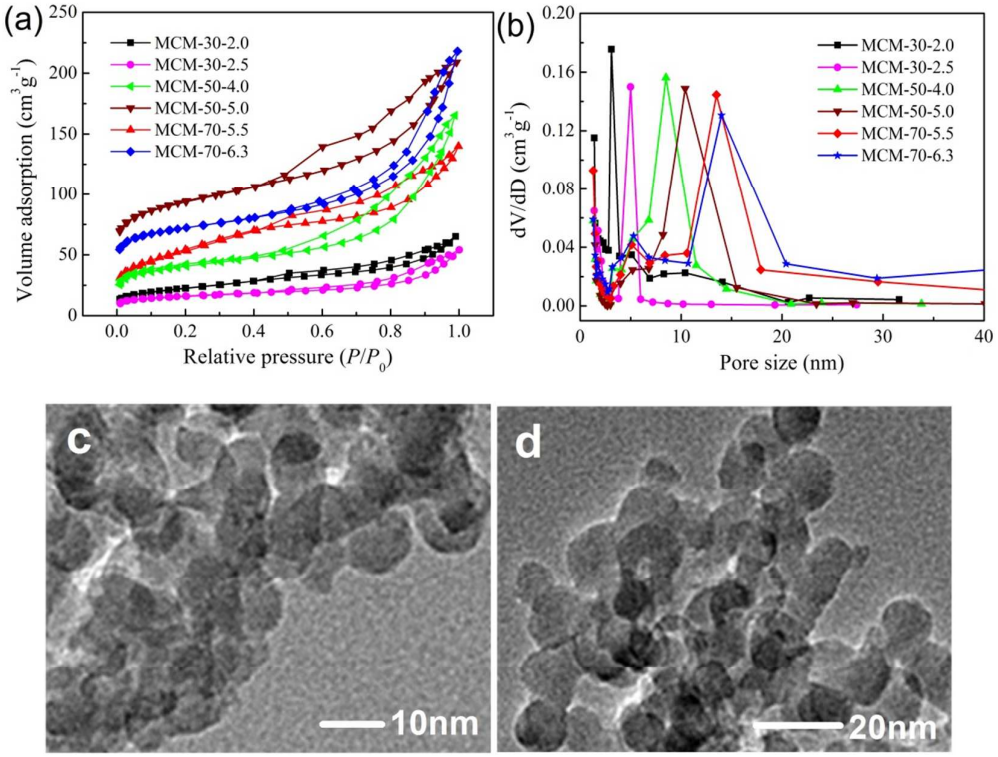

Figure 3. Nitrogen adsorption-desorption isotherms (a), pore size distributions (b) of MCMs, and SiO_2 nanoparticles (c, d).

Table 2. Specific parameters of surface areas, pore sizes and pore volumes of MCMs.

Sample	S_{BET}[a] ($m^2 g^{-1}$)	S_{micr}[b] ($m^2 g^{-1}$)	S_{meso}[c] ($m^2 g^{-1}$)	P[d] (nm)	V_{meso}[e] ($cm^3 g^{-1}$)	V_{tota}[f] ($cm^3 g^{-1}$)
MCM-30-2.0	825	452	373	3.2	0.24	0.74
MCM-30-2.5	806	421	385	5	0.31	0.63
MCM-50-4.0	721	321	400	8.5	0.42	0.66
MCM-50-5.0	789	373	416	10.4	0.47	0.67
MCM-70-5.5	687	308	379	13.5	0.38	0.59
MCM-70-6.3	659	289	370	14	0.44	0.62

[a] The specific surface areas were calculated using BET method; [b] Micropore surface area; [c] Mesopore surface area; [d] The pore diameters were calculated from the adsorption branches of the isotherms by using the BJH model; [e] Mesopore volume; [f] Total pore volume measured at $P/P_0 = 0.99$.

Figure 4a shows XRD patterns of MCMs. Broad diffraction peaks observed at about 2θ=24° and 44° can be indexed as the (002) and (100) planes of amorphous carbon,[37] implying a nongraphitized carbon structure. Figure 4b present Raman spectrum of samples. Two peaks at around 1335 cm^{-1} and 1597 cm^{-1} are assigned to D band and G band of carbon, respectively.[38] The D band reflects crystal defects in carbons and the G band indicates the hexagonal graphitic structure of carbons plane. The relative ratio intensity of D band and G band (I_D/I_G) reflects the degree of graphitization, defects and the domain size of graphitization. Generally, the higher the ratio is, the lower the graphitization degree of the carbons is, the I_D/I_G for amorphous carbon is about 1.0.[39] The estimated I_D/I_G value of MCM-30-2.0, MCM-30-2.5, MCM-50-4.0, MCM-50-5.0 and MCM-70-5.5 are 0.81, 0.82, 0.82, 0.67 and 0.94 respectively, these indicate the samples are mainly disordered carbon coupled with partly graphite layers,

and MCM-50-5.0 with well graphitization structure. One peak at around 2700 cm^{-1} was assigned to G′ band, which is a representative characteristic feature of undisturbed or highly ordered graphitic lattices.[40,41] The existence of the G′ band means more perfection of hexagonal symmetry in the samples, namely, the formation of a partially graphitic structure. MCM-30-2.0, MCM-30-2.5 and MCM-50-5.0 show obvious G′ band, these indicate the well graphitization structure than MCM-50-4.0 and MCM-50-5.5.

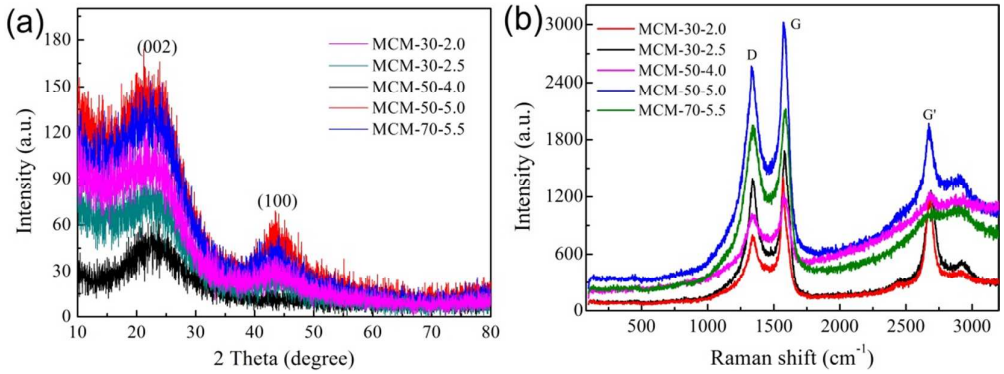

Figure 4. XRD patterns (a), and Raman spectrum (b) of MCMs.

In this study, the carbon microspheres with different mesoporous size on capacitive performances were investigated. EIS measurement was performed to clarify the kinetics at the interface between the electrode and electrolyte, as well as to characterize the contribution of the porous structures to the electrochemical double-layer capacitance.[42,43] Figure 5 shows the Nyquist plot of MCMs measured in 6 M KOH solution in the range of 1 mHz to 10^5 kHz. In the low-frequency region, vertical lines parallel to the imaginary axis are clearly observed, it indicate the excellence of MCMs as electrode materials for supercapaitor because of their highly porous nature. The intermediate frequency region is 45° line in MCMs, which is the characteristic of ion diffusion into the electrode materials. The quasi-semicircle at high

frequency reveals the influence of material porosity and thickness on the migration rate of the ions from the electrolytes inside the porous carbons, and the intercept in the semicircle with the real axis gives the internal resistance (*R*) of the active materials.[44] Generally, a low *R* value means a high ion transfer/diffusion rate into the pores of electrode materials. In this study, the *R* values of MCMs are 0.2-0.5 Ω, it depicts the good transport of electrolyte to the electrolyte/electrode interface of MCMs.

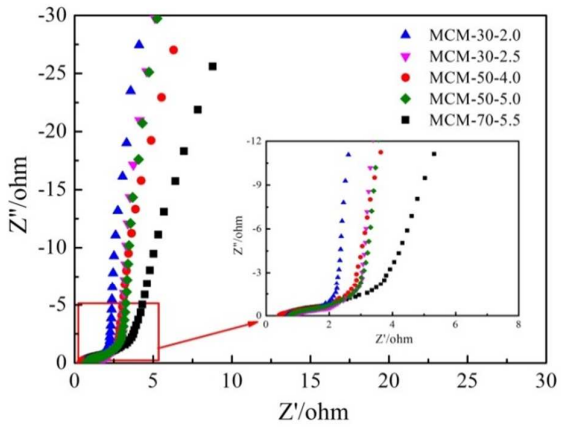

Figure 5. Nyquist plot of MCMs in 6 M KOH solution measured in the range of 1 mHz to 10^5 kHz.

Figure 6 shows the CV curves of MCMs at a scan rate of 50 mV s^{-1} in 6 M KOH aqueous solution. The CV curves exhibit a quasi-rectangular shape at a voltage window of -1.0-0.0 V, which indicate a predominant capacitive behavior with good charge propagation and easy ion transport in the electrode materials.[45] Generally, the specific capacitance is in proportion to CV profile covered areas under the same scan rate and voltage window.[46] Obviously, MCM-30-2.0 and MCM-50-5.0 show relative larger quasi-rectangular areas with good shapes than other samples, it indicates a well electrochemical performance as electrodes materials in 6 M KOH aqueous solution.

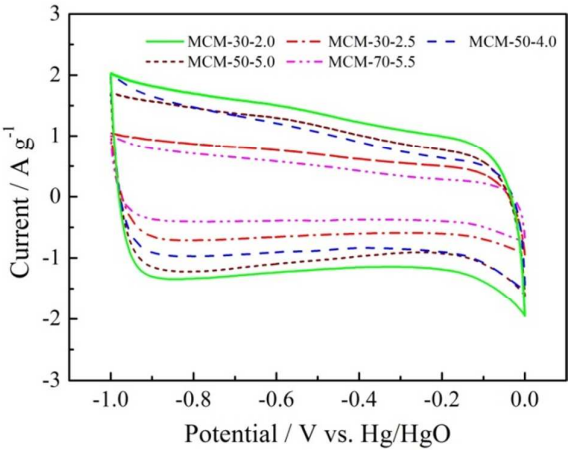

Figure 6. CV curves of MCMs at the scan rate of 50 mV s^{-1} in 6 M KOH aqueous solution.

Figure 7 shows the CV curves of MCM-30-2.0 (Figure 7a) and MCM-50-5.0 (Figure 7b) as electrodes under different scan rates in 6 M KOH aqueous solution. At low scan rates (e.g. 50-100 mV s^{-1}), both of MCM-30-2.0 and MCM-50-5.0 present excellent rectangular shapes because of the electrolyte ions have enough time to move into the nonporous structure of carbon microsphere for electrical double layer formation. However, when the scan rate was increased to 300-800 mV s^{-1}, MCM-30-2.0 shows a distorting rectangular CV shapes, this reflects the resistance of ions motion in the small nanopores which affecting the double layer formation at high scan rates and resulting in the absence of capacitive behavior.[47] While, MCM-50-5.0 presents a relative good quasi-rectangular voltammogram shapes compared with MCM-30-2.0 even at higher scan rates of 500 and 800 mV s^{-1}, which suggests that MCM-50-5.0 can satisfy fast charge/discharge ability due to its larger mesoporous size and surface area for facile diffusion of electrolyte ion and mass transfer.

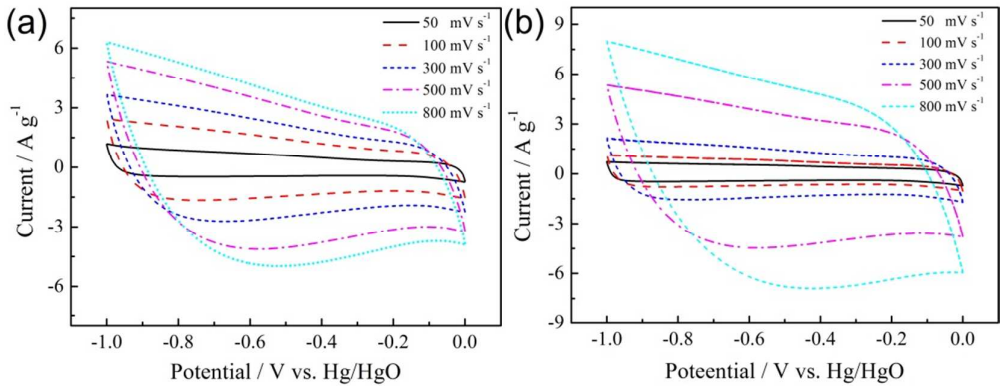

Figure 7. CV curves of MCM-30-2.0 (a) and MCM-50-5.0 (b) under different scan rates.

GCD profiles of MCM-30-2.0 and MCM-50-5.0 under different loading current densities (0.5-20 A g^{-1}) are shown in Figure 8a and Figure 8b. It is noteworthy that both of MCM-30-2.0 and MCM-50-5.0 can remain typical triangle-shaped curves and without obvious ohmic drop even at higher current density of 20 A g^{-1}, which reveals that MCM-30-2.0 and MCM-50-5.0 as electrode materials have a linear galvanostactic charge-discharge performance that are suitable for supercapacitor.

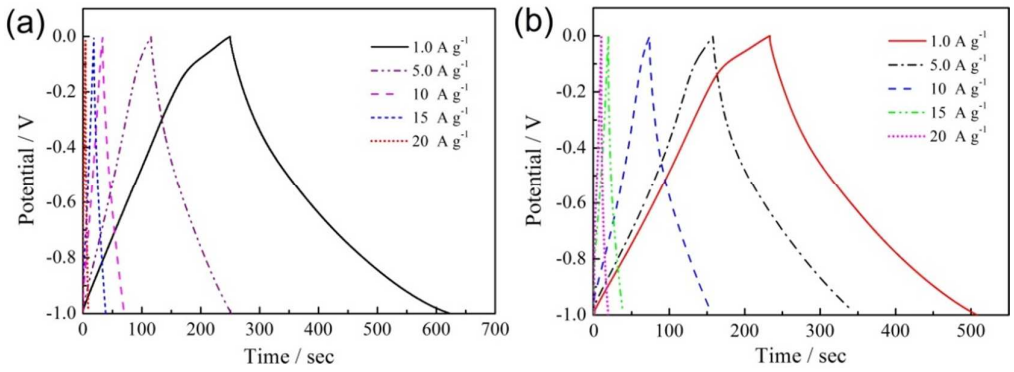

Figure 8. GCD curves of MCM-30-2.0 (a) and MCM-50-5.0 (b) electrode in 6 M KOH solution at different current densities.

Figure 9 shows the specific capacitance of MCM-30-2.0 and MCM-50-5.0 under the current density of 0.5-20 A g^{-1} which calculated from the charge-discharge curves (Figure 8)

according to equation $C_m=It/\Delta Vm$.[48,49] Where C_m is the specific capacitance of supercapacitor (F g^{-1}), m is the mass of material within the electrode (g), I is the charge/discharge current (A), t is the discharge time (s), and ΔV is the potential window (1.0 V) of the charge/discharge (V). Obviously, it was found that at lower current density of 1.0 A g^{-1}, the specific capacitance of MCM-30-2.0 is higher than MCM-50-5.0, this can be attributed to its higher specific surface area of 825 m^2 g^{-1} and pore size of 3.2 nm which benefits to provide abundant sites for adsorbing active ions and enhance the electrochemical capacitance. However, as the current density was increased to 5-20 A g^{-1}, MCM-30-2.0 shows an obvious capacitance drop and MCM-50-5.0 still sustains good capacity, this due to the MCM-50-5.0 with larger mesopore size of 13.5 nm and higher mesoporous surface area of 416 m^2 g^{-1} which could favor the charge transfer process during the fast charge/discharge operation.

Table 3 shows a comparison of the specific capacitances of different forms of carbon materials. Carbon nanotube (MnO_2/CNT) shows an electrochemical capacitance of 169 F g^{-1} at 1.0 A g^{-1}. Carbon nanofibers, such as CNFs exhibit 256 F g^{-1} at 0.2 A g^{-1}, and 170 at 1.0 A g^{-1}. Carbon nanosheets (N-Graphite) show a capacitance of 227 F g^{-1} at 1.0 A g^{-1}, N-functionalization improved the surface wetting properties of the carbon electrode and contributed the enhanced electrochemical performance. As a comparison, HPCMS-2, UCNs and MCM-70-5.5 exhibit 221, 206 and 268 F g^{-1} at 1.0 A g^{-1}. MCM-70-5.5 obtained in this work exhibits a specific capacitance of 268 F g^{-1} at 1.0 A g^{-1}, and 163 F g^{-1} at high current of 20 A g^{-1}. Generally, porous carbon spheres show some advantages, such as regular geometry, adjustable porosity and particle size and good liquidity, which could decrease the resistance of ion diffusion and lead to improved electrochemical performances.[39] In addition, the

homogeneous package among the carbon spheres generates porosity which promotes the formation of ion buffer reservoirs and then reduces the transportation distances of electrolyte ions to the interior carbon surfaces. Therefore, MCMs with homogenous diameter and tunable mesoporous structure show good electrochemical performance.

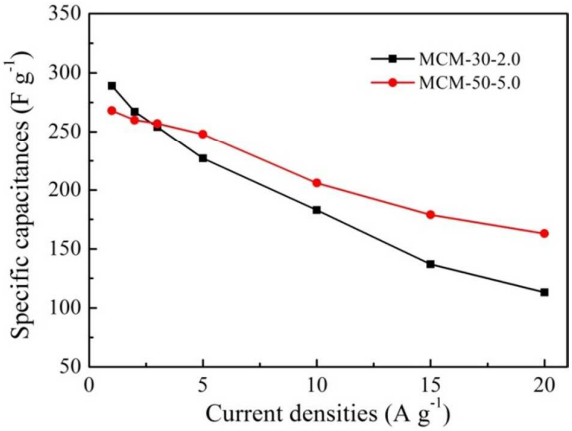

Figure 9. Specific capacitances of MCM-30-2.0 and MCM-50-5.0 under different current densities.

Table. 3 Comparison of the specific capacitances of carbon materials with different forms.

Sample		Capacity (F g^{-1})				S_{BET} (m^2 g^{-1})	Ref
		0.2 A g^{-1}	1 A g^{-1}	20 A g^{-1}	30 A g^{-1}		
Carbon spheres	HPCMS-2		221			709	51
	UCNs		206			842	56
	MCM-70-5.5		268	163		687	This work
Carbon nanosheets	A-CNS		120		104	1957	50
	N-Graphite		227			-	53
	GNS		252			-	59
Carbon nanotubes	A-CNT		145		125	2006	50
	MnO_2/CNT	169				-	54
	CNT		80			200	58
Carbon	N-CNFs	221				-	52

nanofibers	CNFs	256	170	597	55
	CNF		159	277	57

To further understand the electrochemical performances of electrode materials, cycling stability of MCM-30-2.0 and MCM-50-5.0 were conducted at 1.0 A g^{-1} in KOH solution to investigate the specific capacitances and capacity retention. As showing in Figure 10, after 10000 cycle numbers, MCM-30-2.0 and MCM-50-5.0 shows specific capacity of 261 and 254 F g^{-1} with the retention of 90.3%, and 94.7% respectively. The good cycling performance is mainly attributed to the abundant mesoporous structure and double layer charge-discharge process in the electrode materials during the potential cycling test. This result clearly indicates the excellent electrochemical cycling stability of MCM-30-2.0 and MCM-50-5.0, which has high potential for long term applications at lower current density.

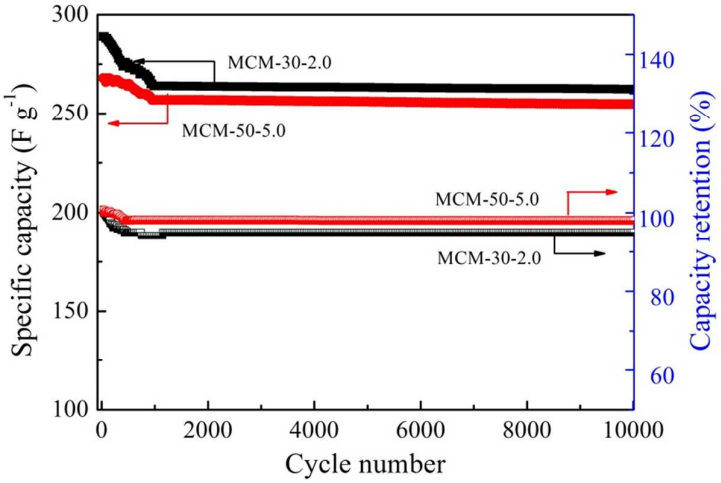

Figure 10. Cycle numbers and capacity retention of MCM-30-2.0 and MCM-50-5.0 at 1.0 A g^{-1}.

4. Conclusion

In summary, carbon microspheres with different mesopore size were prepared by controlling

the size of SiO_2 nanoparticles templates. As-prepared mesoporous carbon microspheres present pore size of 3.2-14 nm and specific areas of 659-872 $m^2 g^{-1}$. As electrode materials for supercapacitor, the results of electrochemical experiments reveal that the typical samples of MCM-30-2.0 and MCM-50-5.0 show specific capacitance of 289 and 268 F g^{-1} under 1.0 A g^{-1}, and specific capacity of 261 and 254 F g^{-1} with the retention of 90.3% and 94.7% after 10000 cycles. When the current density was increased to 20 A g^{-1}, the capacitance remain 113 and 163 F g^{-1} respectively. The results found that a minimal mesopore shows a higher specific capacity under lower current density and relative larger mesopore is convenient for fast charge-discharge process at higher current density.

Acknowledgments

This work was financially supported by the National Natural Science Foundation of China (21207099, 21273162), the Science and Technology Commission of Shanghai Municipality, China (11nm0501000, 12ZR1451100), Key Subject of Shanghai Municipal Education Commission, China (J50102) and Large Equipment Test Foundation of Tongji Universities (2013063, 2013069).

Notes and references

Department of Chemistry, Tongji University, 1239 Siping Road, Shanghai 200092, P. R. China.

*E-mail: ganlh@tongji.edu.cn; liumx@tongji.edu.cn

Tel: +86-21-65982654-8430(extension), Fax: +86-21-65982287

1 G. Wang, L. Zhang, J. Zhang, Chem. Soc. Rev. 2012, 41, 797-828.

2 P. Simon, Y. Gogotsi, Nat. Mater. 2008, 7, 845-854.

3 L. Nyholm, G. Nyström, A. Mihranyan, M. Strømme, Adv. Mater. 2011, 23, 3751-3769.

4 H. C. Chien, W. Y. Cheng, Y.H. Wang, S.Y. Lu, Adv. Funct. Mater. 2012, 22, 5038-5043.

5 H. Jiang, P. S. Lee, C. Li, Energy Environ. Sci. 2013, 6, 41-53.

6 N. Xiao, D. Lau, W. Shi, J. Zhu, X. Dong, H. H. Hng, Q. Yan, Carbon 2013, 57, 184-190.

7 X. He, P. Ling, J. Qiu, M. Yu, X. Zhang, C. Yu, M. Zheng, J. Power Sources. 2013, 240, 109-113.

8 Y. Li, Z. Y. Fu, B. L. Su, Adv. Funct. Mater. 2012, 22, 4634-4667.

9 L. Dai, D. W. Chang, J. B. Baek, W. Lu, Small 2012, 8, 1130-1166.

10 L. L. Zhang, X. S. Zhao, Chem. Soc. Rev. 2009, 38, 2520-2531.

11 S. Chen, J. J. Duan, Y. H. Tang, S. Z. Qiao, Chem. Eur. J. 2013, 19, 7118-7124.

12 Y. Zhai, Y. Dou, D. Zhao, P. F. Fulvio, R. T. Mayes, S. Dai, Adv. Mater. 2011, 23, 4828-4850.

13 C. Merlet, B. Rotenberg, P. A. Madden, P. L. Taberna, P. Simon, Y. Gogotsi, M. Salanne, Nat. Mater. 2012, 11, 306-310.

14 S. Chen, W. Xing, J. J. Duan, X. Hu, S. Z. Qiao, J. Mater. Chem. A. 2013, 1, 2941-2954.

15 Y. Zhu, S. Murali, M. D. Stoller, K. J. Ganesh, W. Cai, P. J. Ferreira, A. Pirkle, R. M. Wallace, K. A. Cychosz, M. Thommes, D. Su, E. A. Stach, R. S. Ruoff1, Science 2011, 332, 1537-1541.

16 M. J. Jung, E. Jeong, Y. Kim, Y. S. Lee, J. Ind. Eng. Chem. 2013, 19, 1315-1319.

17 T. C. Chou, C. H. Huang, R. A. Doong, C. C. Hu, J. Mater. Chem. A. 2013, 1, 2886-2895.

18 Y. Liang, F. Liang, D. Wu, Z. Li, F. Xu, R. Fu, Phys. Chem. Chem. Phys. 2011, 13, 8852-8856.

19 G. Sun, K. Li, L. Xie, J. Wang, Y. Li, Micropor. Mesopor. Mater. 2012, 151, 282-286.

20 W. C. Li, G. Z. Nong, A. H. Lu, H. Q. Hu, J. Porous Mater. 2011, 18, 23-30.

21 Y. Kong, Y. Zhong, X. Shen, S. Cui, M. Yang, K. Teng, J. Zhang, J. Non-Crystalline Solids 2012, 358, 3150-3155.

22 J. Xu, A. Wang, T. Zhang, Carbon 2012, 50, 1807-1816.

23 P. F. Fulvio, R. T. Mayes, X. Wang, S. M. Mahurin, J. C. Bauer, V. Presser, J. M. Donough, Y. Gogotsi, S. Dai, Adv. Funct. Mater. 2011, 21, 2208-2215.

24 W. Stöber, A. Fink, E. J. Bohn, J. Colloid Interface Sci. 1968, 26, 62-69.

25 J. Liu, S. Z. Qiao, H. Liu, J. Chen, A. Orpe, D. Zhao, G. Qing (Max) Lu, Angew. Chem. Int. Ed. 2011, 50, 5947-5951.

26 A. B. Fuertes, P. Valle-Vigo', M. Sevilla, Chem. Commun. 2012, 48, 6124-6126.

27 J. Liu, T. Yang, D. W. Wang, G. Q. Lu, D. Y. Zhao, S. Z. Qiao, Nat. Commun. 2013, 4, 2798, DOI: 10.1038/ncomms3798.

28 J. Qian, M. Liu, L. Gan, P. K. Tripathi, D. Zhu, Z. Xu, Z. Hao, L. Chen, D. S. Wright, Chem. Commun. 2013, 49, 3043-3045.

29 X. Ma, M. Liu, L. Gan, Y. Zhao, L. Chen, J Solid State Electrochem. 2013, 17, 2293-2301.

30 W. Xiong, M. Liu, L. Gan, Y. Lv, Y. Li, L. Yang, Z. Xu, Z. Hao, H. Liu, L. Chen, J. Power Sources. 2011, 196, 10461-10464.

31 K. D. Hartlen, A. P. T. Athanasopoulos, V. Kitaev, Langmuir 2008, 24, 1714-1720.

32 V. M. Masalov, N. S. Sukhinina, E. A. Kudrenko, G. A. Emelchenko, Nanotechnology 2011, 22, 275718 (9pp).

33 X. Ma, M. Liu, L. Gan, P. K. Tripathi, Y. Zhao, D. Zhu, Z. Xu, L. Chen, Phys. Chem.

Chem. Phys. 2014, 16, 4135-4142.

34 C. Tsouris, R. Mayes, J. Kiggans, K. Sharma, S. Yiacoumi, D. DePaoli, S. Dai, Environ. Sci. Technol. 2011, 45, 10243-10249.

35 J. Jin, N. Nishiyama, Y. Egashira, K. Ueyama, Micropor. Mesopor. Mater. 2009, 118, 218-223.

36 D. Tashima, E. Yamamoto, N. Kai, D. Fujikawa, G. Sakai, M. Otsubo, T. Kijima, Carbon 2011, 49, 4848-4857.

37 N. Liu, H. Song, X. Chen, Y. Wang, Mater. Chem. Phys. 2011, 130, 1016-1021.

38 L. Wei, M. Sevilla, A. B. Fuertes, R. Mokaya, G. Yushin, Adv. Funct. Mater. 2012, 22, 827-834.

39 M. Liu, L. Gan, W. Xiong, F. Zhao, X. Fan, D. Zhu, Z. Xu, Z. Hao, L. Chen, Energy Fuels 2013, 27, 1168-1173.

40 J. S. Lee, S. I. Kim, J. C. Yoon, J. H. Jang, ACS Nano 2013, 7, 6047-6055.

41 M. Liu, L. Gan, W. Xiong, Z. Xu, D. Zhu, L. Chen, J. Mater. Chem. A. 2014, 2, 2555-2562.

42 S. H. Aboutalebi, A. T. Chidembo, M. Salari, K. Konstantinov, D. Wexler, H. K. Liu, S. X. Dou, Energy Environ. Sci. 2011, 4, 1855-1865.

43 S. Chen, J. J. Duan, M. Jaroniec, S. Z, Qiao, J. Mater. Chem. A. 2013, 1, 9409-9413.

44 M. Itagaki, Y. Hatada, I. Shitanda, K. Watanabe, Electrochimica Acta 2010, 55, 6255-6262.

45 D. Dan Zhou, Y. J. Du, Y. F. Song, Y. G. Wang, C. X. Wang, Y. Y. Xia. J. Mater. Chem. A. 2013, 1, 1192-1200.

46 B. Xu, F. Wu, R. Chen, G. Cao, S. Chen, Y. Yang, J. Power Sources. 2010, 195,

2118-2124.

47 Q. Zhao, X. Wang, C. Wu, J. Liu, H. Wang, J. Gao, Y. Zhang, H. Shu, J. Power Sources. 2014, 254, 10-17.

48 X. Feng, Y. Liang, L. Zhi, A. Thomas, D. Wu, I. Lieberwirth, U. Kolb, K. Müllen, Adv Funct. Mater. 2009, 19, 2125-2129.

49 Y. Lv, L. Gan, M. Liu, W. Xiong, Z. Xu, D. Zhu, D. S. Wright, J. Power Sources. 2012, 209, 152-157.

50 W. Chen, R. B. Rakhi, M. N. Hedhili, H. N. Alshareef, J. Mat. Chem. A, DOI: 10.1039/C3TA15245F.

51 Q. Zhao, X. Wang, C. Wu, J. Liu, H. Wang, J. Gao, Y. Zhang, H. Shu, J. Power Sources. 2014, 254, 10-17.

52 Y. Fan, Z. Zhao, Q. Zhou, G. Li, X. Wang, J. Qiu, Y. Gogotsi, Carbon 2013, 58 128-133.

53 N. Xiao, D. Lau, W. Shi, J. Zhu, X. Dong, H. Hng, Q. Yan, Carbon 2013, 57, 184-190.

54 W. Zhang, B. Mu, A. Wang, J Mater Sci 2013, 48, 7581-7586.

55 C. Ma, Y. Song, J. Shi, D. Zhang, X. Zhai, M. Zhong, Q. Guo, L. Liu, Carbon 2013, 51, 290-300.

56 Y. Zhao, M. Liu, L. Gan, X. Ma, D. Zhu, Z. Xu, L. Chen, Energy Fuels, 2014, 28, 1561-1568.

57 Z. Tai, X. Yan, J. Lang, Q. Xue, J. Power Sources. 2012, 199, 373-378.

58 D. Y. Kang, J. H. Moon, Appl. Mater. Interfaces 2014, 6, 706-711.

59 Y. R Kang, Y. L. Li, F. Hou, Y. Y. Wen, D. Su, Nanoscale 2012, 4, 3248-3253.